Suppressing Buried Interface Nonradiative Recombination Losses Towards High-efficiency Antimony Triselenide Solar Cells

Guojie Chen, Yandi Luo, Muhammad Abbas, Muhammad Ishaq, Zhuang-Hao Zheng, Shuo Chen, Zhenghua Su, Xianghua Zhang, Ping Fan, Guangxing Liang

Suppressing Buried Interface Nonradiative Recombination Losses Towards High-efficiency Antimony Triselenide Solar Cells

*Guojie Chen, Yandi Luo, Muhammad Abbas, Muhammad Ishaq, Zhuanghao Zheng, Shuo Chen, Zhenghua Su, Xianghua Zhang, Ping Fan, Guangxing Liang**

G. Chen, Y. Luo, M Abbas, Z. M Ishaq, Zheng, S. Chen, Z. Su, P. Fan, G. Liang

Shenzhen Key Laboratory of Advanced Thin Films and Applications, Key Laboratory of Optoelectronic Devices and Systems of Ministry of Education and Guangdong Province, College of Physics and Optoelectronic Engineering

Shenzhen University

Shenzhen, Guangdong 518060, China

Y. Luo and X. Zhang

Institut des Sciences Chimiques de Rennes, UMR 6226

Université de Rennes

Rennes F-35000, France

This article has been accepted for publication and undergone full peer review but has not been through the copyediting, typesetting, pagination and proofreading process, which may lead to differences between this version and the Version of Record. Please cite this article as doi: 10.1002/adma.202308522.

Abstract: Antimony triselenide (Sb_2Se_3) has possessed excellent optoelectronic properties and has gained interest as a light-harvesting material for photovoltaic technology over the past several years. However, the severe interfacial and bulk recombination obviously contribute to significant carrier transport loss thus leading to the deterioration of power conversion efficiency (PCE). In this work, we synergistically employ buried interface and heterojunction engineering to regulate the film growth kinetic and optimize the band alignment. Through this approach, the orientation of the precursor films is successfully

controlled, promoting the preferred orientational growth of the (*hk*1) of the Sb_2Se_3 films. Besides, interfacial trap-assisted non-radiative recombination loss and heterojunction band alignment are successfully minimized and optimized. As a result, the champion device presents a PCE of 9.24% with short-circuit density (J_{SC}) and fill factor (FF) of 29.47 mA/cm^2 and 63.65%, respectively, representing the highest efficiency in sputtered-derived Sb_2Se_3 solar cells. This work provides an insightful prescription for fabricating high-quality Sb_2Se_3 thin film and enhancing the performance of Sb_2Se_3 solar cells.

1. Introduction

The urgent need for high-efficiency, low-cost solar cells has driven the enduring exploration of new light-harvesting materials for thin-film photovoltaics. Being one of the emerging candidates for the second generation of thin-film solar cells like CdTe [1] and $Cu_2(InGa)Se_2$

(CIGS)[2], antimony selenide (Sb_2Se_3) solar cells have attracted substantial research attention. Sb_2Se_3 possesses a one-dimensional crystal structure and remarkable photoelectric properties, such as decent carrier mobility (~ 10 cm^2 V^{-1} S^{-1}), high absorption coefficient ($>10^5$ cm^{-1}), high vapor pressure, low toxicity, and benign grain boundaries without dangling bonds along $(Sb_4Se_6)_n$ ribbons.[3-7] The distinctive crystal structure of Sb_2Se_3 consists of strong covalent bonds in the c-direction (along the one-dimensional chains) and van der Waals (vdW) forces in the a- and b-directions (between the chains), resulting in strong anisotropic electrical and mechanical properties. [8-11] To realize high-efficiency Sb_2Se_3 solar cells, the key lies in achieving an overall high-quality Sb_2Se_3 absorber. However, recent studies have revealed that Sb_2Se_3 solar cells suffer from significant non-radiative recombination losses due to a low-quality absorber layer and complex interfacial defects.[12-16] These losses impair performance close to the Shockley-Queisser limit by adversely affecting charge carrier lifetime and transport efficiency.[17] In order to fully exploit the excellent photoelectric properties of high-efficiency Sb_2Se_3 solar cells, it is imperative to reduce nonradiative recombination losses.

The majority of the contribution to power conversion efficiency (PCE) losses in Sb_2Se_3 thin film solar cells can be attributed to suboptimal interfaces between the absorber and back contact layers and the heterojunction interface. Consequently, substantial efforts have been devoted to modulating the interfacial loss in Sb_2Se_3 thin film solar cells in recent years. The

back-contact interface plays a critical role in determining the back-contact barrier and the growth mechanisms of the absorber layer, which are essential for carrier transport and extraction. For instance, Liang et al. optimized the back barrier height and mitigated the deep-level defects by incorporating a lead selenide (PbSe) as a buried interface between the Mo and Sb_2Se_3 layers, suppressing the non-radiative recombination and enhancing carrier extraction and collection.[18] Similar buried interface modifications using organic molecules and inorganic films have been employed in perovskite solar cells to regulate perovskite crystallization and minimize interfacial recombination.[19-20] Furthermore, in current high-efficiency Sb_2Se_3 solar cells, CdS is commonly used as the electron transport layer (ETL).[21-23] However, there exists poor band alignment between the absorber and ETL. Incorporating doping elements into the buffer layers has been demonstrated as an effective method to regulate doping carrier density and adjust heterojunction band alignment. For example, the addition of $Zn_xCd_{1-x}S$ and In ions into the buffer layers has demonstrated enhanced carrier transport, modified interface band alignment, and increased short-circuit current density. [24-25] Thus, the quality of both the buried interface and heterojunction interface directly influences device performance. However, few studies have simultaneously engineered both interfaces.

In this study, we propose a strategy for a high-efficiency planar heterojunction Sb_2Se_3 solar cell that encompasses both buried interface engineering and heterojunction interface

engineering. To modify the back contact barrier height and suppress non-radiative recombination, we deposit WO_3 films on the Mo glass before sputtering the Sb precursor films. The introduction of WO_3 films as the buried interface optimizes film growth kinetics and reduces defect density, resulting in high-quality Sb_2Se_3 absorber layers. In addition, we utilize heterojunction interface engineering to regulate band alignment and passivate interfacial recombination by doping the CdS layer with Al^{3+}. This doping modification effectively adjusts the band alignment and increases carrier density, leading to improved device performance. Using this dual interface treatment, we achieve high-efficiency Sb_2Se_3 solar cells with a maximum PCE of 9.24%, which represents the highest efficiency among sputtered-derived Sb_2Se_3 solar cells. Our work provides valuable insights into the simultaneous modulation of crystallization, bulk, and interfacial defects through dual interface treatment engineering.

2. Result and discussion

Device Performance

The effect of the dual interface engineering strategy was investigated using a glass/Mo/WO_3/Sb_2Se_3/CdS-Al/ITO/Ag/MgF_2 device configuration (**Figures 1 a and b**), where WO_3 served as the buried interface layer for crystal growth modification. The WO_3 buried layer, denoted as SW15, was directly deposited onto the Mo substrate using thermal

evaporation. Additionally, an Al-doped CdS buffer layer, denoted as SW15-Al, was employed as part of the heterojunction interface treatment. The Al^{3+} solution was spin-coated onto the CdS surface and annealed for 5 minutes to optimize the Sb_2Se_3/CdS interface band alignment and carrier transport (**Figure 1b**). Based on the screening experiment, (**Supplementary Figure 1)**, the optimized thickness of the WO_3 buried layer and the optimized concentration of the $AlCl_3$ solution used in this work are 15 nm and 0.5 M, respectively. The device without any interface modifications is designated as SW0.

The performances of the Sb_2Se_3 solar cell devices were initially investigated under these interface modulations. The current density-voltage (*J-V*) curves of the three types of devices are exhibited in **Figure 1c**. The SW0 device achieved a power conversion efficiency (PCE) of 7.41 % with an open-circuit voltage (V_{OC}) of 0.473 V, short current density (J_{SC}) of 26.77 mA/cm^2, and fill factor (FF) of 58.43 %. In the case of buried interface modification, the V_{OC}, J_{SC}, and FF slightly increased to 0.484 V, 28.59 mA/cm^2, and 59.36 %, respectively, resulting in a PCE of 8.25 %. With the dual interface modification, the SW15-Al device showed further enhancements in the PV parameters, reaching a V_{OC} of 0.492 V, J_{SC} of 29.47 mA/cm^2, and FF of 63.65 %, resulting in a PCE of 9.24 %, representing the highest efficiency in sputtered-derived Sb_2Se_3 solar cells (**Table 1**). Based on the statistical results of the PV parameters of those devices (**Supplementary Figures 2 and 3**), it can be demonstrated the outstanding reproducibility of the developed process and the device demonstrated exceptional

stability as the overall PCE scarcely changed throughout the testing period. The corresponding external quantum efficiency (EQE) spectra and the integrated J_{SC} are shown in **Figure 1d**, which confirms the trends observed in the *J-V* measurements. The superior photon response for the buried interface modification device in the wavelength of 550 to 900 nm signifies that the WO_3 buried interface modulation has improved the quality of the Sb_2Se_3 layer, as well as optimized the contact quality between the absorber and the Mo substrate. This will be discussed in more detail later. In comparison to the other device, the photon response after dual interface modification is greatly improved in the visible region of 400–600 nm. It is conceivable that the modified CdS buffer layer improved the J_{SC} by reducing recombination at the Sb_2Se_3/CdS-Al interface as well as reducing absorption loss. Furthermore, the decreasing trend in the Urbach energy (E_U) of the devices (**Figure 1e**) further authenticates that no matter whether the single modification case or the dual modification case, the nonradiative recombination is reduced due to the deep-level defect passivation. By integrating the EQE value, the band gaps of the buffer layer and the absorber layer of different devices are obtained, respectively (**Supplementary Figure 4 and Supplementary Table 1**). It is evident that the Al-doping had a slight effect on increasing the bandgap of the CdS buffer layer, resulting in improved response. On the other hand, the buried layer did not significantly alter the bandgap of the Sb_2Se_3 layer; it only exhibited minor variations.

Morphological, Structural, and Interface Analyses.

Based on the known association between preferred orientation and carrier transport efficiency in the Sb_2Se_3 bulk, the relationship between the substrate temperature and the Sb precursor film was investigated. As demonstrated by X-ray diffraction (XRD) measurements in **Figure 2a**, an increase in substrate temperature during the sputtering process leads to a notable shift in the diffraction peaks. Initially, the peaks shift from the (104) orientation to the (003) orientation and eventually transition to the (012) orientation. The fact that the (003) peak's diffraction intensity at a substrate temperature of 250 ℃ is much higher than that of the other sample implies that the film tends to grow along the vertical (001) orientation. We further checked the morphology of the Sb precursor film and found a compact and smooth morphology for all samples, except the 250 ℃ sample with the particle-like structure on the surface (**Supplementary Figure 5)**. Moreover, a tiny particle-like structure on the surface of the film at 250 ℃ was witnessed by atomic force microscopy (AFM) images (**Supplementary Figure 6**), which might be attributed to the change in orientation of the precursor film. The root-mean-square roughness (R_q) of the precursor reduced to 3.85 nm from 24.85 nm, when the preferred orientation shifted to (003), indicating that the Sb precursor tended to grow along the (001) vertical direction. We then deposited the Sb precursor film with different thicknesses of the WO_3 buried layer to study its influence on the orientation of the Sb film, as depicted in **Figure 2b.** The influence of the buried layer

thickness on the preferred orientation of the Sb film was found to be negligible; however, it has an impact on the crystallinity of the Sb film. Thus, an optimized Sb precursor film was subjected to a post-selenization process to synthesize the Sb_2Se_3 thin film. As shown in **Figure 2c**, the XRD measurements exhibited almost similar patterns for all samples, which is in good agreement with the JCPDS standard card (No. 15–0861) of the orthorhombic phase of Sb_2Se_3 without any detectable impurities and the space group of this card is Pbnm (62). From the XRD pattern, the 15 nm WO_3 buried layer sample had the highest (221) and (002) diffraction peaks. **Supplementary Figure 7** provides a visual representation of the full width at half-maximum (FWHM) values for the (211), (221), and (002) diffraction peaks of all the samples. In comparison to the SW0 and SW15 samples, the FWHM values of (211), (221), and (002) diffraction peaks showed a decrease from 0.343, 0.351, and 0.378 to 0.341, 0350, and 0.363, respectively. Obviously, the (002) diffraction peak intensity significantly increased while the FWHM value decreased after careful optimization. This significant increase in intensity and decrease in FWHM suggests a substantial improvement in the crystallinity of the material after the modification of the buried interface. Furthermore, we calculated the texture coefficient (TC) to intuitively quantify the favorable orientation of the Sb_2Se_3 thin film (**Supplementary Figure 8**), and the fitting detail is provided in **Supplementary Note 1**. The larger the TC value of the (*hkl*) diffraction peak, the more favorable orientation along this direction. [26-27] For the SW15 sample, the TC value of (*hk*1)

orientation is higher than that of the other sample. Thus, by preserving the other vertical (211) and (221) orientations, the (002) orientation was effectively induced. Therefore, we preliminarily believe that the improvement of the device performance is probably related to the preferred orientation of the absorber layer.

To further gain deep insight into the film growth process with or without the WO_3 buried layer treatment, the top-view and cross-section images were characterized via scanning electron microscope (SEM). To understand the grain growth mechanism upon selenization of the Sb film, the selenization process is briefly described in the following four stages[28]: (1) Se powder first melts into the liquid stage and then diffuses as Se gas. (2) the Se vapor first reacted with the Sb precursor film surface, then inducing the formation of the Sb_2Se_3 crystal nucleus. (3) With the Se pressure increasing, more Se vapor diffuses along the $(Sb_4Se_6)_n$ gap of the Sb_2Se_3 film, and Se completely reacts with the Sb precursor from the surface to the bottom forming the Sb_2Se_3. (4) the Sb_2Se_3 grain continues to grow until the end of the process. The schematic representation of the selenization treatment is depicted in **Supplementary Figure 9**. The top-view and cross-section SEM images show us a two-layer structure at the beginning of the post-selenization process, consisting of a top and a bottom grain layer. (**Figure 2d and Supplementary Figure 10)**. These results demonstrated that the first and second reaction processes are finished at the heating-up stage. As the selenization duration was prolonged to 5 min, the surface grain size gradually increased, and the bottom

grain layer grew simultaneously. Obviously, due to the compositional competition between the top and bottom grain layers, some pinholes appeared between the two layers in the SW0-5 min sample. For the SW15-5 min sample, the top grain layer merges with the bottom grain layer to form a single-layered film comprised of larger grains. These findings demonstrate that the presence of the WO_3 buried layer would not only prevent the Se vapor from diffusing downward to inside Mo, reducing the reaction with Mo to bring up a thinner $MoSe_2$ layer but also likely suppress the nucleation of small particles and forming large grains under the same selenization duration. The samples prepared with 10 min (SW0) and further prolonged selenization process also caused the two-layer grain to merge into a single layer, but the size and number of pinholes that appeared at the Sb_2Se_3/Mo interface also increased, which would be detrimental to device performance. By contrast, under the same case, the SW15 sample presents a smoother and more compact surface, which is beneficial for the device's performance. Moreover, as shown in **Supplementary Figure 11**, the detailed frequency histograms versus grain size distribution indicate that the average grain size rose from 1.5 μm in the SW0 sample to 1.7 μm in the SW15 sample.

We further employed electron backscatter diffraction (EBSD) to investigate the in-plane orientations in the microstructure of the Sb_2Se_3 thin film. The EBSD image is depicted in **Figure 2e**, with the colored orientation IPF maps inset in it and the morphology of the EBSD sample is shown in **Supplementary Figure 12**. The EBSD image exhibits a dominant red

color, signifying a quasi-(001) orientated growth in the Sb_2Se_3 film. This orientation is promising for charge carrier transport, ensuring improved device performance. This is one of the main factors contributing to the noticeable enhancement in the device's J_{SC} (short-circuit current) attributed to buried interface modulation.[29] Moreover, photoluminescence (PL) spectroscopy was employed to study the radiative recombination of the Sb_2Se_3 layer. **Figure 2f** and **Supplementary Figure 13** illuminate the temperature-dependent PL spectra, which were recorded under temperatures from 10 K to 300 K. It can be observed that the two sample shows similar thermal quenching behavior. This quenching of the PL spectra is due to the non-recombination centers in the Sb_2Se_3 film, with increasing temperature.[30-31] Obviously, the SW15 sample presents a slower PL quenching rate, demonstrating that there are fewer non-radiative recombination centers in the SW15 sample. The findings signify that the buried layer treatment largely optimized the film growth process, leading to a high-quality absorber layer with preferential orientation and larger grain, and reducing the density of non-radiative recombination centers at the same time. Moreover, both PL emission peaks shift to lower energies as the temperature decreases. Temperature and the variation of PL maximum peak energy are shown in **Figure 2g**. Based on Levanyuk and Osipov's model for disordered semiconductors, α has a strong relationship with the carrier concentration.[30] The SW15 sample exhibited a gentler red shift rate, indicating an enhancement of carrier concentration for the Sb_2Se_3 thin film with the buried layer treatment.[30]

We further conducted the Kelvin probe force microscopy (KPFM) analysis to examine the surface potential distribution of the Sb_2Se_3 and CdS film. The KPFM images of the SW0 and SW15 films shown in **Figures 3a, and 3b** reveal that the contact potential difference (CPD) distribution of SW0 and SW15 are −200 to −120 and −300 to −170 mV, respectively. In addition, the average CPD of SW15 and SW0 film is −232 and −161 mV, respectively (**Figure 3c**). The SW15 film exhibits a lower CPD distribution, reflecting a lower Fermi level.[32] For P-type material, the downshift of the Fermi level means the increment of the carrier concentration. When contact with the N-type material forms the P-N junction, a lower Fermi level would lead to a larger band bending, thus resulting in a higher V_{OC}.[33-35] Similarly, the KPFM measurement was also employed to study the enhancement of electrical properties of the CdS film with or without doping treatment. **Figure 3d, e** depicted the AFM image of the CdS and CdS-Al film, respectively, and the KPFM images of these are shown in **Figure 3e, h**, respectively. The contact potential difference (CPD) distribution of CdS and CdS-Al samples is −70 to 10 and 110 to 240 mV, respectively. CPD values at the grain boundary (GBs) and grain surface (GS) differ when compared (**Figure 3f, i**), suggesting that the grain boundaries may serve as the primary pathway for ion movement. [36-37] For the CdS sample, the CPD fluctuation between GBs and GS was estimated to be 50 mV. In contrast, the CPD fluctuation was estimated to be 30 mV for the CdS-Al sample. The lower fluctuation not only represented the more efficient charge carrier separated along the $[Sb_4Se_6]_n$ ribbons,

but also demonstrated effective passivation of the detrimental surface defects and interface states.[38-39] The larger CPD value for CdS-Al in **Supplementary Figure 14** denotes the upshift of the Fermi level, which indicates that the Al doping treatment has favorably increased the carrier concentration.[40] Moreover, the higher Fermi level would cause a relatively larger band bending, hindering the hole at the front interface and leading to a larger V_{OC} as well. In brief, the higher the carrier concentration, the faster the carrier transport, and this is the key factor for higher device performance.

Ultraviolet photoelectron spectroscopy (UPS) analysis was employed to further exhibit the physical mechanisms and obtain more comprehensive information about the band alignment, which dramatically affects the charge transport mechanism. **Supplementary Figure 15** shows the valence band maximum (VBM) and the secondary electron cut-off (E_{cutoff}) spectra for the SW0 film, SW15 film, and the CdS film with and without Al-doping. The work function (W_F) and VBM can be estimated by extrapolating the linear portion, the details are shown in **Supplementary Note 2**. Notably, the W_F mentioned here is the quasi-Fermi level. Based on these estimations, the band alignment diagram is demonstrated in **Figures 3j to 3l**. All the Sb_2Se_3 films present a P-type feature. With the WO_3 buried interface treatment, the VBM of the SW15 film is shifted up, indicating the Fermi level is relatively closer to the VBM. Furthermore, the Fermi level of the CdS-Al (–4.28 eV) is relatively higher than that of the CdS (–4.93 eV), which is consistent with the KPFM analysis. We further check the

conduction band offset (CBO) to quantify the band alignment at the heterojunction. Usually, the positive CBO is recorded as the spike-like type (0 ~ 0.3 eV), while the negative CBO is recorded as the cliff-like type (–0.1 to –0.3).[41] Both the SW0/CdS and the SW15/CdS heterojunction present a cliff-like type, implying that there is more serious interface recombination. Cliff is known to have little effect on photogenerated electrons, but it does reduce the activation energy for carrier recombination at the interface.[13] Under the forward bias, a cliff would serve as a barrier to injected electrons, leading to the majority of carriers recombining via defects at the interface, thereby worsening the device performance. By contrast, a spike-like CBO can be obtained at the SW15/CdS-Al heterojunction, forming the barriers that prohibit charge carriers from reaching the heterojunction interface, thus preventing charge carriers from accumulating near the interface. These results verify that SW15/CdS-Al heterojunction can effectively passivate the interface recombination and greatly promote the charge carrier collection to enhance the J_{SC} of the device.

Transmission electron microscope (TEM) characterization was conducted to gain insight into the interface properties and grain orientations of the champion Sb_2Se_3 device with dual interface treatment. **Figure 4a** illustrates the cross-section image of the device, showing compact and firmly adherent features, which would be beneficial for reducing current leakage and preventing recombination of the interfacial carriers. The high-resolution TEM (HRTEM) image of a chosen region of Sb_2Se_3/CdS heterojunction (the yellow box in Figure 4a) is

demonstrated in **Figure 4b**. With the dual interface treatment, the optimal heterojunction presents less lattice mismatch between the absorber and buffer layer. **Figures 4b1 and b2** illustrate the atomic resolution high angle annular dark field scanning transmission electron microscopy (HAADF-STEM) images obtained at the CdS side (yellow box in Figure 4b) and Sb_2Se_3 side (blue box in Figure 4b), respectively. The measured crystal spacing is predicted to be 0.328 nm, which is comparable with the (111) crystal spacing of the CdS, and hexagonal lattice sites can be observed as well. **Figure 4b2** displays the HAADF-STEM image of the Sb_2Se_3 region at a higher magnification (15.5 Mx), which was carried out with Gaussian blur processing to lower the noise level and produce a clearer atomic arrangement. 1D crystal structure on the atomic scale consisting of $(Sb_4Se_6)_n$ nanoribbons packed parallelly in the [001] direction can be witnessed. The crystal spacing of 0.316 nm corresponds to the (211) crystal space of Sb_2Se_3. This indicates that the Sb_2Se_3 grain is quasi (001)-oriented vertically, which is crucial to enhance the charge carrier transfer mechanism. The energy-dispersive X-ray spectroscopy (EDS) mapping of the buffer layer is shown in **Figure 4c,** which demonstrates how Al doping treatment only modified the upper layer of the CdS buffer (The dark bit presents the area where the Al doping concentrates mainly). Generally, heating up organic solvents would cause them to volatilize. In this work, most of the Cl ions would react with hydrogen ions and finally volatilize as gaseous hydrogen chloride upon the CdS annealing treatment. The annealing process is quite moderate (295 $^{\circ}$C and 5 minutes) so

that significant Cl diffusion within the CdS buffer would be difficult to occur. On the other hand, Cl doping would turn the Sb_2Se_3 film into an N-type, according to Hobson's report.[42] In our case, no variation of valence/conduction band position and fermi level has been found in the Sb_2Se_3 thin film upon Al doping treatment in the CdS buffer, as depicted in **Figure 3k-l**. Therefore, we conservatively assume that Cl ions did not diffuse into the Sb_2Se_3 layer all the way from the top side of the CdS buffer. According to our previous work[3], we believe that the majority of the aluminum ions are distributed on the surface of CdS, and a minor portion of them take over the original Cd atoms in the CdS lattice under the influence of thermal diffusion. In addition, the EDS results (Figure 4d) further confirm that the WO_3 buried interface treatment could reduce the reaction between Mo and Se. The enlarged image of the green box in Figure 4d is shown in **Figure 4e**. We find that the lattice fringes are clear and the estimated crystal spacing is 0.387 nm, corresponding to the (002) crystal space of WO_3.[43] The WO_3 buried interlayer probably enables the $Mo/WO_3/Sb_2Se_3$ back contact to have a quasi-Ohmic contact rather than a Schottky contact, leading to the improvement in carrier transport.

Photoelectric Properties and Trap States Investigation

To evaluate the photoelectric properties of the absorber layer and their impact on the photovoltaic performance, we conducted dark *J-V* measurements on the device. The dark *J-V* curves can be found in **Supplementary Figure 16** and the detailed calculation is provided in

Supplementary Note 3. Comparing the device with dual interface treatment to the SW0 and SW15 devices, lower series resistance (R_s) and ideality factor (A) values indicated a suppressed defect recombination at the interface and in bulk regions. Additionally, the SW15-Al device showed a lower reverse saturation current density (J_0), indicating a reduction in nonradiative recombination loss due to a lower deep defect concentration.[44] To further analyze this, we used the space charge-limited current (SCLC) technique to precisely measure the defect state density (**Supplementary Figure 17, and the computational method is shown in Supplementary Note 4**). Based on the formula, it can be observed that the calculated defect density (N_{trap}) values of the SW0, SW15, and SW15-Al devices are 2.75 $\times 10^{14}$ cm^{-3}, 2.36$\times 10^{14}$ cm^{-3}, and 2.06$\times 10^{14}$ cm^{-3}, respectively. This demonstrates that a lower defect recombination concentration signifies better absorber quality and improved defect passivation effectiveness.

To further understand the superior performance of the device with dual interface modification, temperature-dependent *J-V* measurement (*J-V-T*) was employed under dark conditions (**Supplementary Figure 18)**. The SW0 device showed a suppressed diode-like behavior with the reduction in temperature, while the devices with single or dual interface treatments maintain strong diode characteristics, designating a reduction in the transmission barrier with these treatments. To quantify the temperature-dependent series resistance (R_S) of the devices, we plotted the *J-V-T* curves (**Supplementary Figure 19**). The R_S of the SW0

device grew dramatically up to ten times, which is double the SW15 and SW15-Al devices. This divergence in R_S towards decreasing temperature implies that the barrier height, which prevents charge carrier transit, is caused by both a blocking barrier and the background series resistance.[45-46] Moreover, by plotting ln(R_ST) versus 1/T (**Figure 5a,** the details are given in **Supplementary Note 5**), we determined the back contact diode barrier height (Φ_B). The Φ_B value for the SW15 sample was 92.7 meV, lower than that of the SW0 sample (165.5 meV), indicating a reduced barrier height for buried interface treatment. Furthermore, the dual interface treatment resulted in a barrier height of 68.2 meV, further optimizing carrier transport and improving device performance. The crossover behavior seen in the light and dark *J-V* data further confirms the existence of the Schottky barrier (**Supplementary Figure 20)**. Specifically, the crossover behavior occurs at a higher current for the SW15 and SW15-Al devices, suggesting lower barrier heights compared to the SW0 device, consistent with the *J-V-T* results. Overall, the reduction of the back contact barrier height is a crucial factor in enhancing charge carrier transport. Additionally, the *J-V-T* data allows us to determine the recombination path in the device. By plotting Aln(J_0) against 1/kT (**Figure 5b**), we can estimate the activation energy of interface recombination (E_A). The value of E_A can indicate the dominance of either bulk or interface recombination.[46] A low E_A value compared to the band gap suggests dominant interface recombination. For the SW0 device, the E_A value was 1.14 eV, lower than the band gap, indicating the prevalence of interface

recombination. The SW15 and SW15-Al devices had E_A values of 1.21 and 1.25 eV, respectively, which were close to the band gap. This suggests that with single or dual interface modulation, interface recombination was significantly suppressed, resulting in better P-N junction quality and a lower back contact barrier.

Capacitance-voltage (*C*-*V*) profiling and deep-level capacitance profiling (DLCP) measurements were conducted to further investigate the influence of interfacial recombination (**Figure 5c**, **Supplementary Note 6**). The estimated interfacial defect concentration of the SW0, SW15, and SW150-Al are 6.96×10^{16} cm^{-3}, 1.46×10^{16} cm^{-3}, and 7.52×10^{15} cm^{-3}, respectively, confirming that the single or dual interface treatment would substantially decrease the interfacial defect concentration for higher P-N junction quality. The variation in carrier concentrations between low and high frequencies reflects the number of bulk defects. The DLCP curves under high and low frequencies of the three devices estimated bulk defect concentration of the SW0, SW15, and SW150-Al are 7.61×10^{15} cm^{-3}, 5.91×10^{15} cm^{-3}, and 2.72×10^{15} cm^{-3}, respectively (**Supplementary Figure 21**). The obtained built-in voltage (V_{bi}) values of SW0, SW15, and SW15-Al through C^{-2}-V analysis are 0.458 V, 0.556 V, and 0.768 V respectively. Higher V_{bi} is considered more conducive to accelerating the transport of the charge carrier, thus leading to improved V_{OC} and J_{SC} (**Supplementary Figure 22**).[47] Moreover, the decreased space charge region (SCR) width could be related to the enhanced doping density, consistent with the UPS results, while a

lower W_d might help to reduce recombination inside the SCR, improving V_{OC} **(Supplementary Note 6**).

Deep-level transient spectroscopy (DLTS) studies are employed to analyze the bulk defect properties of the device, including defect density (N_T), defect capture cross-section (σ), and defect activation energy (E_T). All the devices exhibit two DLTS signals, with both negative and positive peaks, where the positive and negative peaks can be attributed to majority carrier traps and minority carrier traps, respectively, showing one electron trap (E1) and one hole trap (H1) for our device (**Supplementary Note 7, Figure 5d**).[48-49] The detailed defect parameters, such as N_T, σ and E_T, were obtained by linearly fitting the points near the DLTS peak on the Arrhenius curves, where each defect demonstrates similar activation energy in both devices, signifying a common origin (**Figure 5e**). Additionally, the first-principle theoretical calculations reveal that the E1 defect corresponds to selenium vacancy (V_{Se1}) and the H1 defect corresponds to selenium antistites (Se_{Sb1}) (**Figure 5g**).[47] The energy band structure and defect levels in three devices were studied to assess the impact of the defect on device performance (**Figures 5h-i**). Deep-level defects near the middle of the band gap are more likely to become recombination centers compared to shallow defects near the band edge. The selenium antistites (Se_{Sb1}) defect is an amphoteric defect, with similar carrier capture cross-sections for both holes and electrons, significantly affects Fermi-level pinning

and Shockley-Read-Hall (SRH) recombination, thereby hindering carrier transport and lowering the overall photovoltaic performance.[12]

On the other hand, the H1 defect, located near the middle of the band gap, functions as the primary recombination center in the device. In the SW0 device, the larger capture cross-section of H1 results in severe trap-assisted recombination and substantial carrier losses. Upon introducing the interface treatment, the capture cross-section values for the H1 defect decrease, while the N_T values slightly increase or remain unchanged. Since the capture cross-section is tiny, the carriers are re-emitted quickly after being trapped in this shallow state. Despite the slight increase in N_T, the capture cross-section values are smaller than those of the dual-interface treatment devices, indicating the main optimization achieved through dual-interface treatment. Similarly, for the E1 defect, the SW15-Al device exhibits a smaller defect density compared to the SW0 device, along with a one-order of magnitude reduction in capture cross-section, consistent with its superior film quality. Furthermore, the product of the capture cross-section and defect density ($\sigma \cdot N_T$) as a measure of the impact of deep-level defects on the device performance shows that trap lifetime (τ_{trap}) is inversely proportional to the value of $(\sigma \cdot N_T)^{-1}$ (**Figure 5f**, **Table 2)**.[50] The trap lifetime is utilized to describe the ability of the defect to trap the holes, if the defect is occupied by the hole, it is more likely to function as an efficient recombination center and shorten the capture lifetime. The values of $\sigma \cdot N_T$ for the E1 and H1 defects were significantly reduced, indicating a prolonged trap

lifetime associated with nonradiative recombination of electrons and holes through defects or trap states. For the H1 defect, although the SW15-Al device had a higher defect density than the SW15 device, its smaller capture cross-section and longer capture lifetime make it more difficult to become an effective recombination center thus enabling better performance. Overall, introducing dual-interface treatments substantially decreases the defect density and captures cross-section, improving film quality, which explains the enhanced device performance.

Carrier Recombination Dynamics Analysis

The charge-carrier dynamics were assessed to understand the optoelectronic processes, which affect its performance and determine its photovoltage, photocurrent, and fill factor. The *J-V* measurements were carried out under different illumination light intensities to investigate the charge extraction ability of the devices. The slopes on a double logarithmic scale should be near 1 when the device is not experiencing space-charge limited current.[51] Here, the SW15-Al device has the highest slope value compared to the SW0 and SW15 devices, demonstrating faster charge extraction efficiency for the SW15-Al device (**Figure 6a**). Additionally, the interfacial charge transfer properties assessed by electrical impedance spectroscopy (EIS) are presented as Nyquist plots with the corresponding equivalent circuit (**Supplementary Figure 23)**. The SW0 device shows the largest internal resistance (R_S) and the smallest recombination resistance (R_{rec}), suggesting severe charge recombination without

any interface treatments (**Supplementary Table 2**). On the other hand, the SW15-Al device shows the largest R_{rec} and the smallest R_S, indicating that the interface modulations have effectively passivated charge recombination and promoted charge transport.

Moreover, according to the diffusion-recombination model ($\tau_n = R_{rec} \times C$),[52] the lifetime is increased to 2.8 ms for the SW15-Al device, which can effectively reduce recombination and improve carrier transport due to excellent crystallization of the absorbing layers. The charge transfer and recombination properties were further studied by transient photocurrent (TPC) and transient photovoltage (TPV) experiments (**Figures 6b and 6c**). The TPC decay time (τ_{TPC}) and TPV recombination lifetime (τ_{TPV}) are estimated by fitting decay curves, where the τ_{TPC} under 0 bias for the SW15-Al device (0.368 μs) is dramatically decreased compared to the SW0 (0.624 μs) and SW15 (0.512 μs) devices, indicating faster charge transport and higher J_{SC}. Similarly, the photovoltage decay lifetime for the SW15-Al device increased from 0.549 ms to 1.21 ms after dual interface treatments, signifying the effective passivation of non-radiative recombination. Moreover, the modulated transient photocurrent and photovoltage (M-TPC/TPV) characterizations were employed to estimate the bias voltage-dependent charge extraction (η_{ext}) and charge collection (η_C) efficiencies, which quantify the charge loss of the devices. The η_C may be related to the interfacial recombination and metal-semiconductor contact performance, while the η_{ext} may be related to the absorber recombination.[53] The SW15 and SW15-Al devices exhibit higher η_C than the SW0 device

during the entire voltage regime and are remotely close to 100% before 0.3 V bias voltage (**Figure 6d**). With the increasing bias voltages, the η_C of the SW0 device significantly decreases to ~ 90%, while the η_C of SW15 and SW15-Al devices decreases more slowly and maintains ~ 96% at 0.5 V bias voltage, suggesting the suppressed charge recombination. It is evident that all three devices present a similar decreased tendency in η_{ext}, but the SW15-Al device exhibits the highest η_{ext} than that of the SW0 and SW15 devices, indicating an improvement in the absorber quality (**Figure 6e**). It is anticipated that the dual interface treatments contribute to the device performance improvement by suppressing charge recombination and enhancing the absorber quality.

The charge transfer kinetics were studied by transient absorption spectroscopy (TAS), where TAS mapping demonstrates a distinct photoinduced absorption (PIA) peak at 720 nm for both samples, indicating the capture of photo-generated minority carriers (**Figure 6g-i**).[7] The decay kinetics at 720 nm wavelength for both samples are shown in **Figure 6f**. The kinetics are fitted by the bi-exponential equation,[50] with the detailed fitting parameters summarized in **Supplementary Note 8** and **Table 3**. In particular, the fast component (τ_1) represents the interface/surface recombination and the long decay component (τ_2) is assigned to the bulk defect recombination. The carrier lifetimes for the SW0, SW15, and SW15-Al samples were 1847.33 ps, 3106.33 ps, and 8714.58 ps, respectively. Notably, the dual interface modulations significantly increased both decay components, indicating more effective extraction and

collection of carriers in the Sb_2Se_3 device. Moreover, the interface and bulk recombination were substantially suppressed, particularly the dominant bulk recombination, which aligns well with the DLTS results. Overall, the efficient buried interface treatment and heterojunction treatment optimized Sb_2Se_3 absorber growth engineering, resulting in a preferred (hk1) orientation, longer carrier lifetime, and improved band alignment. These optimized parameters are certainly the dominant reasons behind the enhanced performance of the solar cell.

3. Conclusion

In conclusion, we demonstrated a simple and effective strategy of dual interface engineering. Remarkably, we discovered that the buried interface modification of WO_3 not only induced a striking (*hk*1) orientation of the Sb precursor, thereby regulating the kinetics of Sb_2Se_3 film growth, but also notably mitigated deep-level defects in the films. As a result, non-radiative recombination was suppressed, and the carrier lifetime was prolonged. Additionally, the WO_3 buried interface minimized the barrier height blocking between Mo and Sb_2Se_3, thus increasing the carrier transport efficiency. Likewise, the Al-doped CdS treatment at the heterojunction interface optimized the energy band alignment with suitable energy offsets for effective charge extraction and reduced interface recombination. Combining these two interface treatments, we effectively inhibited interfacial and SCR recombination, towards enhanced carrier transport efficiency and an extended lifetime. Consequently, this

simultaneous modulation enabled a device efficiency of 9.24%, representing the highest value for sputtered Sb_2Se_3 solar cells. Thus, our work offers new insights for guiding orientation control of the Sb_2Se_3 film and improving the efficiency of Sb_2Se_3 solar cells.

4. Experimental Section

Sb_2Se_3 thin film deposition

The Sb_2Se_3 layers were synthesized by a two-step method on the Mo/WO_3 or Mo substrate, in which we combine radiofrequency (RF) magnetron sputtering deposition and post-selenization for fabrication. In this work, the WO_3 layer was introduced to be the buried interface between the Sb_2Se_3 and the Mo substrate using thermal evaporation techniques. WO_3 powder was used as the evaporation source. The base vacuum was pumped to 8×10^{-4} Pa. The quartz crystal microbalance was used to monitor the thickness and the evaporation rate. The thickness was controlled from 10 to 20 nm, and the rate was about 0.2 Å/s. After that, the Mo/WO_3 sample was removed from the evaporation chamber and placed inside the sputtering chamber to deposit the Sb precursor thin film. The base vacuum of the sputtering chamber was 8×10^{-4} Pa. The substrate temperature was fixed at 250 °C to grow highly (003)-textured Sb film. The sputtering power and the working pressure were kept at 30 W and 1.0 Pa, respectively. The Sb target was purchased from ZhongNuo Advanced Material（Beijing）Technology Co., Ltd. The sputtering duration was kept at 45 min to obtain about 750

nm Sb precursor film. Then, the Sb sample was placed into the vacuum quartz tube furnace for selenization. Before beginning selenization, high-purity argon (Ar) gas was introduced into the tube to remove the residual impurity gas. The weight of 0.2 g high-purity Se powder (ZhongNuo Advanced Material（Beijing）Technology Co., Ltd) was placed inside the two ceramic crucibles on both sides of the Sb samples. The selenization temperature was fixed at 415 °C with a heating rate of 20 °C min^{-1}, and the duration of selenization ranged from 0 to 15 min. The working pressure was kept at 2.5 mtorr during the selenization. Once the heating program finished, the furnace lid was opened for faster cooling.

Solar cell fabrication

According to our previous recipe[28], the CdS buffer layer was deposited on the $Mo/WO_3/Sb_2Se_3$ sample using a chemical bath deposition (CBD). In this process, the precursor solution of $CdSO_4$ (0.015 M), thiourea (0.75 M), and ammonium hydroxide (⩾ 28%) was employed. The deposition temperature was kept at 80 °C for 9 min. The Al^{3+} solution (0.5 M) was obtained by dissolving the $AlCl_3$ into the organic solvent of 2-methoxy ethanol. For doping treatment, the solution was spin-coated on the surface of the CdS layer and then combined with annealing on the hot plate for 5 min. Indium tin oxide (ITO) window layers were then deposited onto the surface of the CdS layer via magnetron sputtering. To complete the device, the silver (Ag) electrodes were deposited by thermal evaporation to

form metallic contact. Finally, the surface of the device was divided into small squares with an identical active area of 0.075 cm^2.

Film and device characterizations

A scanning electron microscope characterized the top-view and cross-sectional images of the Sb_2Se_3 thin film (SEM, SUPPA 55). Raman spectroscopies were collected under an excitation wavelength of 532 nm. The crystal structure and phase of the Sb_2Se_3 and Sb films were studied by X-ray diffraction (XRD, Ultima-iv, CuK_α radiation under operation conditions of 40 kV and 40 mA from 10° to 60°). Photoluminescence spectra (PL) were characterized using a He-Cd laser low-temperature fluorescence spectrum measurement system with an excited wavelength of 442 nm. Atomic force microscope (AFM) and Kelvin probe force microscope (KPFM) images were performed by a Bruker Multimode 9. Electron backscatter diffraction (EBSD) characterization was conducted by QUANTAX CrystAlign 400i (Bruker). Ultraviolet Photoelectron Spectroscopy (UPS) was performed by PHI 5000 Versa Probe III with He I source (21.22 eV) under an applied negative bias of 9.0 V. Transmission electron microscopy (TEM) images were performed by an FEI Titan Cubed Themis G2 300 microscope, and the focused ion beam (FIB, FEI Scios) was utilized to prepare the sample for TEM imaging. Transient absorption spectroscopy (TAS) spectra were characterized via a transient absorption spectrometer (Newport), equipped with a Spectra-Physics Solstice Ace regenerative amplifier (800 nm wavelength, 100 fs pulses with

1 kHz repetition rate). The decay kinetics were fitted by a biexponential model $\gamma = \Sigma A_i \exp(-x/t_i)$ and the carrier lifetime (τ) was obtained by $\tau = \Sigma A_i t_i^2 / \Sigma A_i t_i$ (i = 2). The Janis VPF-800 cryostat controller-equipped FT-1030 HERA DLTS system was employed to characterize the deep-level transient spectroscopy (DLTS) spectra. The Current density-voltage (*J-V*) measurement of the Sb_2Se_3 thin film solar cell was characterized by a source meter under AM 1.5 G simulated irradiation illumination (100 mW cm^{-2}). The external quantum efficiency (EQE) value was collected by a QE/IPCE measurement system (Zolix Solar Cell Scan 100) and incident light was calibrated using a monocrystalline silicon diode. A Keithley 4200A-SCS system was employed to measure the Capacitance Voltage (*C-V*) and drive-level capacitance profiling (DLCP). Temperature-dependent dark *J-V* (*J-V-T*) characterization was performed through the Keithley 4200A-SCS system, equipped with a Lakeshore 325 temperature controller to maintain the various temperature conditions. The electrochemical impedance spectroscopy (EIS) characterization was measured with frequencies ranging from 1Hz to 100 kHz using an electrochemical workstation (CHI660e). A laboratory-built setup at Key Laboratory for Renewable Energy was introduced to obtain the electricity-modulated transient photovoltage and photocurrent (M-TPV/M-TPC) spectra.[53] A 532 nm pulse laser (Brio, 20Hz, 4 ns) was utilized to excite the solar cell, and the decay process was detected by a digital oscilloscope (Tektronix, DPO 7104).

Supporting Information

Supporting Information is available from the Wiley Online Library or from the author.

Acknowledgments

This work was supported by the National Natural Science Foundation of China (No. 62074102), Guangdong Basic and Applied Basic Research Foundation (2022A1515010979) China, Science and Technology plan project of Shenzhen (20220808165025003) China. The authors wish to acknowledge the assistance on (TEM/STEM/FIB) received from the Electron Microscope Center of Shenzhen University.

Conflict of Interest

The authors declare no conflict of interest.

Data Availability Statement

The data that support the findings of this study are available from the corresponding author upon reasonable request.

Keywords

Sb_2Se_3, carrier transport, non-radiative recombination losses, solar cell, efficiency

Received: ((will be filled in by the editorial staff))

Revised: ((will be filled in by the editorial staff))

Published online: ((will be filled in by the editorial staff))

Reference

[1] J. M. Burst, J. N. Duenow, D. S. Albin, E. Colegrove, M. O. Reese, J. A. Aguiar, C. S. Jiang, M. K. Patel, M. M. Al-Jassim, D. Kuciauskas, S. Swain, T. Ablekim, K. G. Lynn, W. K. Metzger, *Nat. Energy*, **2016**, 1, 16015.

[2] M. Nakamura, K. Yamaguchi, Y. Kimoto, Y. Yasaki, T. Kato, H. Sugimoto, *IEEE J. Photovoltaics*, **2019**, 9, 1863-1867.

[3] Z. Li, X. Liang, G. Li, H. Liu, H. Zhang, J. Guo, J. Chen, K. Shen, X. San, W. Yu, R. E. I. Schropp, Y. Mai, *Nat. Commun.*, **2019**, 10, 125.

[4] Y. Zhao, S. Wang, C. Li, B. Che, X. Chen, H. Chen, R. Tang, X. Wang, G. Chen, T. Wang, J. Gong, T. Chen, X. Xiao, J. Li, *Energy Environ. Sci.*, **2022**, 15, 5118-5128.

[5] G. Liang, M. Chen, M. Ishaq, X. Li, R. Tang, Z. Zheng, Z. Su, P. Fan, X. Zhang, S. Chen, *Adv. Sci.*, **2022**, 9, 2105142.

[6] X. Wen, C. Chen, S. Lu, K. Li, R. Kondrotas, Y. Zhao, W. Chen, L. Gao, C. Wang, J. Zhang, G. Niu, J. Tang, *Nat. Commun.*, **2018**, 9, 2179.

[7] R. Tang, S. Chen, Z. H. Zheng, Z. H. Su, J. T. Luo, P. Fan, X. H. Zhang, J. Tang, G.-X. Liang, *Adv. Mater.*, **2022**, 34, 2109078.

[8] P. Fan, G. J. Chen, S. Chen, Z. H. Zheng, M. Azam, N. Ahmad, Z. H. Su, G. X. Liang, X. H. Zhang, Z. G. Chen, *ACS Appl. Mater. Interfaces*, **2021**, 13, 46671-46680.

[9] V. Steinmann, R. Brandt, T. Buonassisi, *Nat. Photonics*, **2015**, 9, 355-357.

[10] Z. Duan, X. Liang, Y. Feng, H. Ma, B. Liang, Y. Wang, S. Luo, S. Wang, R. E. I. Schropp, Y. Mai, Z. Li, *Adv. Mater.*, **2022**, 34, 2202969.

[11] C. Chen, L. Wang, L. Gao, D. Nam, D. Li, K. Li, Y. Zhao, C. Ge, H. Cheong, H. Liu, H. Song, J. Tang, *ACS Energy Lett.*, **2017**, 2, 2125-2132.

[12] W. Lian, R. Cao, G. Li, H. Cai, Z. Cai, R. Tang, C. Zhu, S. Yang, T. Chen, *Adv. Sci.*, **2022**, 9, 2105268.

[13] S. Chen, Y. Fu, M. Ishaq, C. Li, D. Ren, Z. Su, X. Qiao, P. Fan, G. Liang, J. Tang, *InfoMat*, **2023**, 5, e12400.

[14] B. Che, Z. Cai, P. Xiao, G. Li, Y. Huang, R. Tang, C. Zhu, S. Yang, T. Chen, *Adv. Mater.*, **2023**, 35, 2208564.

[15] S. Wang, Y. Zhao, L. Yao, C. Li, J. Gong, G. Chen, J. Li, X. Xiao, *Sci. Bull.*, **2022**, 67, 263-269.

[16] G. J. Chen, R. Tang, S. Chen, Z. H. Zheng, Z. H. Su, H. L. Ma, X. H. Zhang, P. Fan and G. X. Liang, *ACS Appl. Mater. Interfaces*, **2022**, 14, 31986-31997.

[17] F. H. Alharbi, S. Kais, *Renewable Sustainable Energy Rev.*, **2015**, 43, 1073-1089.

[18] X. Liang, Y. Feng, W. Dang, H. Huang, X. Wang, Y. Guo, K. Shen, R. E. I. Schropp, Z. Li, Y. Mai, *ACS Energy Lett.*, **2023**, 8, 213-221.

[19] X. Zhang, W. Qiu, S. Apergi, S. Singh, P. Marchezi, W. Song, C. Sternemann, K. Elkhouly, D. Zhang, A. Aguirre, T. Merckx, A. Krishna, Y. Shi, A. Bracesco, C. van Helvoirt, F. Bens, V. Zardetto, J. D'Haen, A. Yu, G. Brocks, T. Aernouts, E. Moons, S. Tao, Y. Zhan, Y. Kuang, J. Poortmans, *ACS Energy Lett.*, **2023**, 8, 2532-2542.

[20] M. Wang, W. Wu, Y. Liu, S. Yuan, D. Tian, C. Zhang, Z. Ma, J. Deng, J. Chen, Z. Lou, W. Li, J. Fan, *Adv. Funct. Mater.*,**2023**, 2300700.

[21] G. X. Liang, Y. D. Luo, S. Chen, R. Tang, Z. H. Zheng, X. J. Li, X. S. Liu, Y. K. Liu, Y. F. Li, X. Y. Chen, Z. H. Su, X. H. Zhang, H. L. Ma, P. Fan, *Nano Energy*, **2020**, 73, 104806.

[22] R. Tang, Z. H. Zheng, Z. H. Su, X. J. Li, Y. D. Wei, X. H. Zhang, Y. Q. Fu, J. T. Luo, P. Fan, G. X. Liang, *Nano Energy*, **2019**, 64, 103929.

[23] Y. Zhao, S. Wang, C. Jiang, C. Li, P. Xiao, R. Tang, J. Gong, G. Chen, T. Chen, J. Li, X. Xiao, *Adv. Energy Mater.*, **2022**, 12, 2103015.

[24] C. Chen, X. Liu, K. Li, S. Lu, S. Wang, S. Li, Y. Lu, J. He, J. Zheng, X. Lin, J. Tang, *Appl. Phys. Lett.*, **2021**, 118, 172103.

[25] S. Chen, T. Liu, M. Chen, M. Ishaq, R. Tang, Z. Zheng, Z. Su, X. Li, X. Qiao, P. Fan, G. Liang, *Nano Energy*, **2022**, 99, 107417.

[26] S. Rijal, D.-B. Li, R. A. Awni, C. Xiao, S. S. Bista, M. K. Jamarkattel, M. J. Heben, C.-S. Jiang, M. Al-Jassim, Z. Song, Y. Yan, *Adv. Funct. Mater.*, **2022**, 32, 2110032.

[27] Z. Li, X. Chen, H. Zhu, J. Chen, Y. Guo, C. Zhang, W. Zhang, X. Niu, Y. Mai, *Sol. Energy Mater. Sol. Cells*, **2017**, 161, 190-196.

[28] Y. D. Luo, R. Tang, S. Chen, J. G. Hu, Y. K. Liu, Y. F. Li, X. S. Liu, Z. H. Zheng, Z. H. Su, X. F. Ma, P. Fan, X. H. Zhang, H. L. Ma, Z. G. Chen, G. X. Liang, *Chem. Eng. J.*, **2020**, 393, 124599.

[29] X. Wen, Z. Lu, B. Li, G.-C. Wang, M. A. Washington, Q. Zhao, T. M. Lu, *Chem. Eng. J.*, **2023**, 462, 142026.

[30] Q. Yan, Q. Sun, H. Deng, W. Xie, C. Zhang, J. Wu, Q. Zheng, S. Cheng, *J. Energy Chem.*, **2022**, 75, 8-15.

[31] J. Zhou, X. Xu, B. Duan, H. Wu, J. Shi, Y. Luo, D. Li, Q. Meng, *Nano Energy*, **2021**, 89, 106405.

[32] S. Ye, H. Rao, M. Feng, L. Xi, Z. Yen, D. H. L. Seng, Q. Xu, C. Boothroyd, B. Chen, Y. Guo, B. Wang, T. Salim, Q. Zhang, H. He, Y. Wang, X. Xiao, Y. M. Lam, T. C. Sum, *Nat. Energy*, **2023**, 8, 284-293.

[33] J. Wang, J. Zhou, X. Xu, F. Meng, C. Xiang, L. Lou, K. Yin, B. Duan, H. Wu, J. Shi, Y. Luo, D. Li, H. Xin, Q. Meng, *Adv. Mater.*, **2022**, 34, 2202858.

[34] H. Si, Q. Liao, Z. Kang, Y. Ou, J. Meng, Y. Liu, Z. Zhang, Y. Zhang, *Adv. Funct. Mater*, **2017**, 27, 1701804.

[35] Y. Zhou, L. Wang, S. Chen, S. Qin, X. Liu, J. Chen, D. J. Xue, M. Luo, Y. Cao, Y. Cheng, E. H. Sargent, J. Tang, *Nat; Photonics*, **2015**, 9, 409-415.

[36] Y. Shao, Y. Fang, T. Li, Q. Wang, Q. Dong, Y. Deng, Y. Yuan, H. Wei, M. Wang, A. Gruverman, J. Shield, J. Huang, *Energy Environ. Sci.*, **2016**, 9, 1752-1759.

[37] Z. Kang, H. Si, M. Shi, C. Xu, W. Fan, S. Ma, A. Kausar, Q. Liao, Z. Zhang, Y. Zhang, *Sci. China Mater.*, **2019**, 62, 776-789.

[38] W. Yang, J. H. Kim, O. S. Hutter, L. J. Phillips, J. Tan, J. Park, H. Lee, J. D. Major, J. S. Lee, J. Moon, *Nat. Commun.*, **2020**, 11, 861.

[39] C. Chen, K. Li, S. Chen, L. Wang, S. Lu, Y. Liu, D. Li, H. Song, J. Tang, *ACS Energy Lett.*, **2018**, 3, 2335-2341.

[40] L. Lou, Y. Gong, J. Zhou, J. Wang, X. Xu, K. Yin, B. Duan, H. Wu, J. Shi, Y. Luo, D. Li, H. Xin, Q. Meng, *J. Energy Chem.*, **2022**, 70, 154-161.

[41] Z. Su, G. Liang, P. Fan, J. Luo, Z. Zheng, Z. Xie, W. Wang, S. Chen, J. Hu, Y. Wei, C. Yan, J. Huang, X. Hao, F. Liu, *Adv. Mater.*, **2020**, 32, 2000121.

[42] T. D. C. Hobson, L. J. Phillips, O. S. Hutter, H. Shiel, J. E. N. Swallow, C. N. Savory, P. K. Nayak, S. Mariotti, B. Das, L. Bowen, L. A. H. Jones, T. J. Featherstone, M. J. Smiles, M. A. Farnworth, G. Zoppi, P. K. Thakur, T.-L. Lee, H. J. Snaith, C. Leighton, D. O. Scanlon, V. R. Dhanak, K. Durose, T. D. Veal, J. D. Major, *Chem. Mater.*, **2020**, 32, 2621.

[43] C. Liu, K. Shen, D. Lin, Y. Cao, S. Qiu, J. Zheng, F. Bao, Y. Gao, H. Zhu, Z. Li, Y. Mai, *ACS Appl. Mater. Interfaces*, **2020**, 12, 38397-38405.

[44] G.X. Liang, C.H. Li, J. Zhao, Y. Fu, Z.X. Yu, Z.H. Zheng, Z.H. Su, P. Fan, X.H. Zhang, J.T. Luo, L. Ding, S. Chen, *SusMat*, **2023**, 3, 682.

[45] O. Gunawan, T. K. Todorov, D. B. Mitzi, *Appl. Phys. Lett.*, **2010**, 97, 233506.

[46] Y. Zhao, Z. Yu, J. Hu, Z. Zheng, H. Ma, K. Sun, X. Hao, G. Liang, P. Fan, X. Zhang, Z. Su, *J. Energy Chem.*, **2022**, 75, 321-329.

[47] C. Chen, J. Tang, *ACS Energy Lett.*, **2020**, 5, 2294-2304.

[48] R. Tang, X. Wang, W. Lian, J. Huang, Q. Wei, M. Huang, Y. Yin, C. Jiang, S. Yang, G. Xing, S. Chen, C. Zhu, X. Hao, M. A. Green, T. Chen, *Nat. Energy*, **2020**, 5, 587-595.

[49] D. Liu, R. Tang, Y. Ma, C. Jiang, W. Lian, G. Li, W. Han, C. Zhu, T. Chen, *ACS Appl. Mater. Interfaces*, **2021**, 13, 18856-18864.

[50] W. Lian, C. Jiang, Y. Yin, R. Tang, G. Li, L. Zhang, B. Che and T. Chen, *Nat. Commun.*, **2021**, 12, 3260.

[51] J. Zheng, C. Liu, L. Zhang, Y. Chen, F. Bao, J. Liu, H. Zhu, K. Shen, Y. Mai, J. Zheng, C. Liu, K. Shen, Y. Mai, *Chem. Engin. J.*, **2022**, 446, 136474.

[52] P. A. Fernandes, A. F. Sartori, P. M. P. Salomé, J. Malaquias, A. F. da Cunha, M. P. F. Graça, J. C. González, *Appl. Phys. Lett.*, **2012**, 100, 233054.

[53] J. Zhou, X. Xu, H. Wu, J. Wang, L. Lou, K. Yin, Y. Gong, J. Shi, Y. Luo, D. Li, H. Xin, Q. Meng, *Nat. Energy*, **2023**, 8, 526-535.

Table 1 Comparison of planar heterojunction Sb_2Se_3 solar cells with different fabrication methods.

Method	Device configuration	*Eff* (%)	V_{OC} (mV)	J_{SC} (mA/cm^2)	*FF* (%)	Ref
Co-eva	Mo/Sb_2Se_3/CdS/ZnO/AZO/Ag	4.25	427	17.11	58.15	[27]

CSS	$Mo/MoSe_2/Sb_2Se_3/TiO_2/CdS/ZnO/ZnO:Al$	9.2	400	32.52	70.3	[3]
IVD	$Mo/MoSe_2/Sb_2Se_3/CdS/AZO/i\text{-}AZO$	10.12	488	30.86	67.19	[10]
RTE	$ITO/CdS/Sb_2Se_3/PbS\ QDs/Au$	6.50	427	25.50	59.3	[11]
VTD	$ITO/CdS/Sb_2Se_3/Au$	7.60	420	29.90	60.4	[6]
Hydrothermal	$FTO/CdS/Sb_2Se_3/Spiro\text{-}O\ MeTAD/Au$	7.89	449	28.3	62.1	[49]
CBD	$FTO/CdS/Sb_2Se_3/Spiro\text{-}O\ MeTAD/Au$	10.57	467	33.52	67.64	[4]
Sput-Se	$Mo/Sb_2Se_3/CdS/ITO/\ Ag$	6.06	494	25.91	47.7	[22]
Sput-Sb-Se	$Mo/Sb_2Se_3/CdS/ITO/\ Ag$	6.15	455	22.75	59.5	[28]
Sput-Sb-Se	$Mo/Sb_2Se_3/CdS/ITO/\ Ag$	6.84	504	24.91	54.47	[21]
Sput-Sb-Se	$Mo/Sb_2Se_3/CdS/ITO/\ Ag$	8.64	520	27.8	59.8	[7]
Sput-Sb-Se	$Mo/Sb_2Se_3/CdS/ITO/\ Ag$	9.24	492	29.47	63.65	This work

Co-eva: Co-evaporation. CSS: Closed space sublimation. IVD: Injection vapor deposition RTE: Rapid thermal evaporation. VTD: Vapor transport deposition. CBD: Chemical bath deposition. Sput-Se: Sputtering and selenization.

Table 2 The trap energy level (E_T), capture cross-section (σ), trap concentration (N_T), and $N_T \times \sigma$ of the detected defects in the three devices.

Sample	Defects	E_T (eV)	σ (cm^2)	N_T (cm^{-3})	$N_T \times \sigma$ (cm^{-1})
SW0	E1	E_C–0.291	8.93×10^{-18}	1.06×10^{13}	9.47×10^{-5}
	H1	E_V+0.369	1.12×10^{-17}	1.40×10^{14}	1.57×10^{-3}
SW15	E1	E_C–0.285	7.16×10^{-18}	9.11×10^{12}	6.52×10^{-5}
	H1	E_V+0.347	4.59×10^{-18}	1.36×10^{14}	6.24×10^{-4}
SW15-Al	E1	E_C–0.231	4.41×10^{-19}	5.23×10^{12}	2.31×10^{-6}

H1	E_V+0.305	1.57×10^{-18}	1.68×10^{14}	2.64×10^{-4}

Table 3 Results of biexponential fitting of decay kinetics curves.

Sample	A_1	τ_1	A_2	τ_2	τ_{ave}
SW0	0.38	76.72	0.62	1891.35	1847.33
SW15	0.30	99.55	0.70	3147.10	3106.33
SW15-Al	0.26	120.22	0.74	8756.04	8714.58

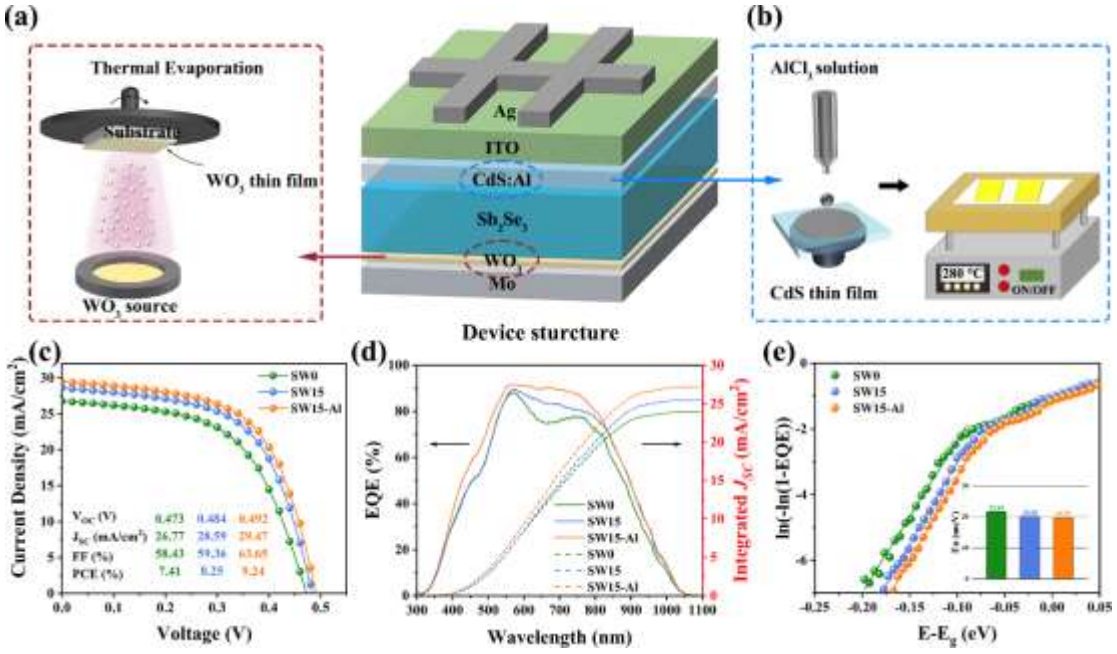

Fig. 1 Schematic diagram of production procedure and device photovoltaic performance. (a) Schematic diagram of deposition of the WO_3 buried interface layer. (b) Schematic diagram of Al ion doping treatment of the CdS buffer layer. (c) *J-V* curves and EQE spectra of SW0, SW15, and SW15-Al samples. (e) Urbach energy was derived from the EQE data of three samples.

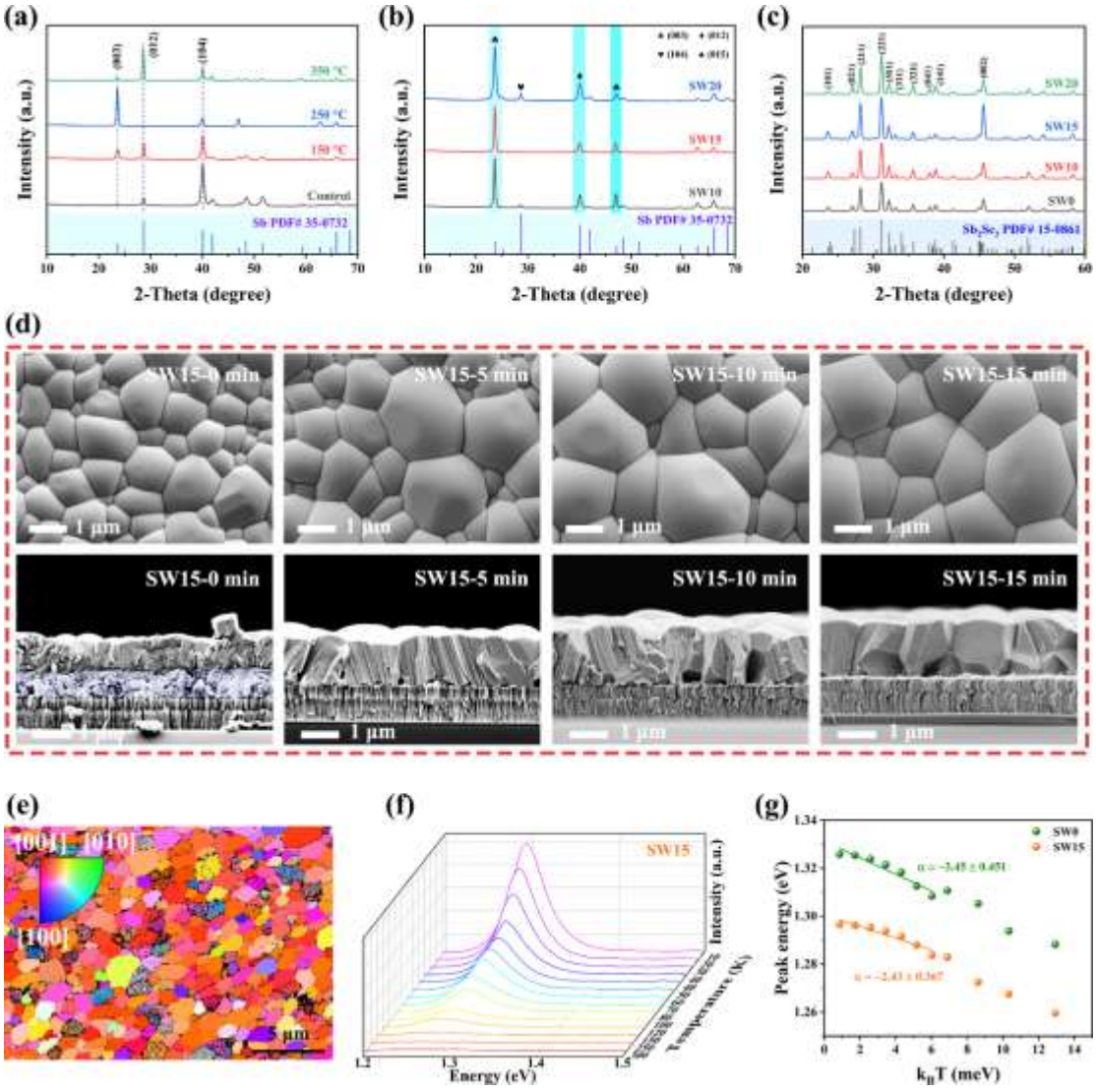

Fig. 2 Influence of buried interface engineering on the film growth kinetics. (a) XRD patterns of Sb precursor film with different substrate temperatures. (b) XRD patterns of Sb precursor film with different thicknesses of WO_3 layers. (c) XRD patterns of Sb_2Se_3 film with different thicknesses of WO_3 layers. (d) Surface morphology SEM images and cross-sectional SEM images of the Sb_2Se_3 (SW15) films at different selenization times. (e) Electron backscatter diffraction (EBSD) crystallographic orientation mapping for the SW15 films (IPF-Z

component). (f) Temperature-dependent PL curves of SW15 film. (g) Variation of PL maximum peak energy under different temperatures.

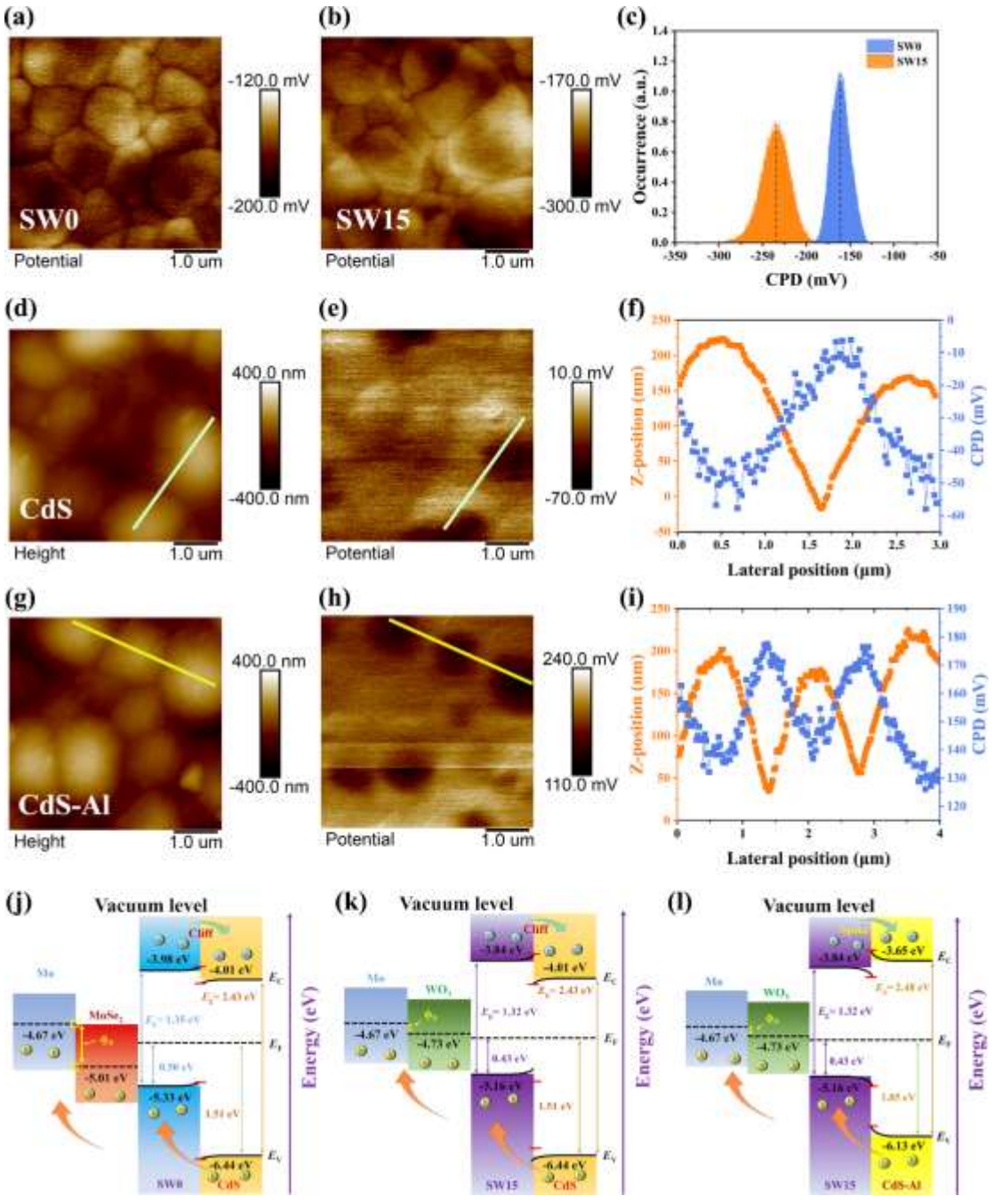

Fig. 3 Surface potential and band alignment. Kelvin probe force microscopy (KPFM) images of the (a) SW0 film and (b) SW15 film. (c) Contact potential difference (CPD) distribution of SW0 and SW15 films. Atomic force microscopy (AFM) images of (d) pristine CdS film, and (g) CdS-Al film. KPFM images of (e) pristine CdS film, and (h) CdS-Al film. Line profiles extracted from the AFM and contact potential difference map for (f) pristine CdS film and (i) CdS-Al film. Schematic diagram of the band alignment for (j) SW0 device, (k) SW15 device, and (I) SW15-Al device.

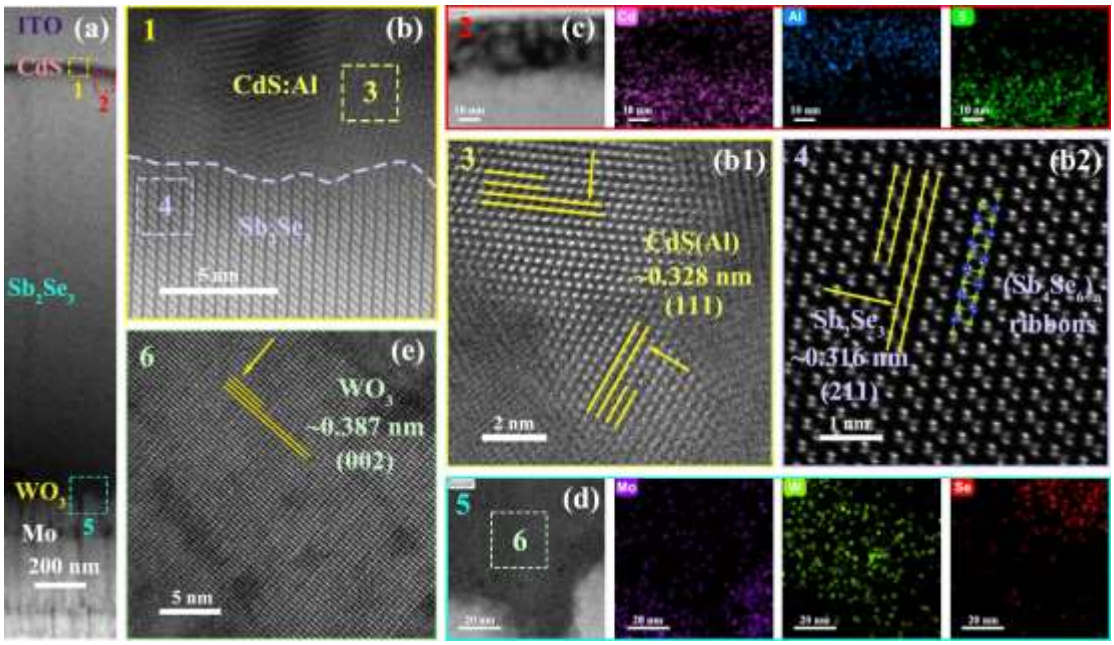

Fig. 4 TEM characterization of the champion SW15-Al device with dual interface modulations. (a) Cross-sectional TEM image of the device. (b) HRTEM image of the selected area near the Sb_2Se_3/CdS heterojunction interface (yellow box in (a), labeled as 1). (b1) HAADF-STEM image with Gaussian blur treatment of the CdS buffer layer (yellow box in (b), labeled as 3). (b2) HAADF-STEM image with Gaussian blur treatment of the Sb_2Se_3 layer (blue box in (b), labeled as 4). (c) Cross-sectional TEM image and mapping analysis of the selected area near the Sb_2Se_3/CdS heterojunction interface (red box in (a), labeled as 2).

(d) Cross-sectional TEM image and mapping analysis of the selected area near the WO_3/Sb_2Se_3 interface (blue box in (a), labeled as 5). (e) HAADF-STEM image with Gaussian blur treatment of the WO_3 buried interface (green box in (d), labeled as 6)

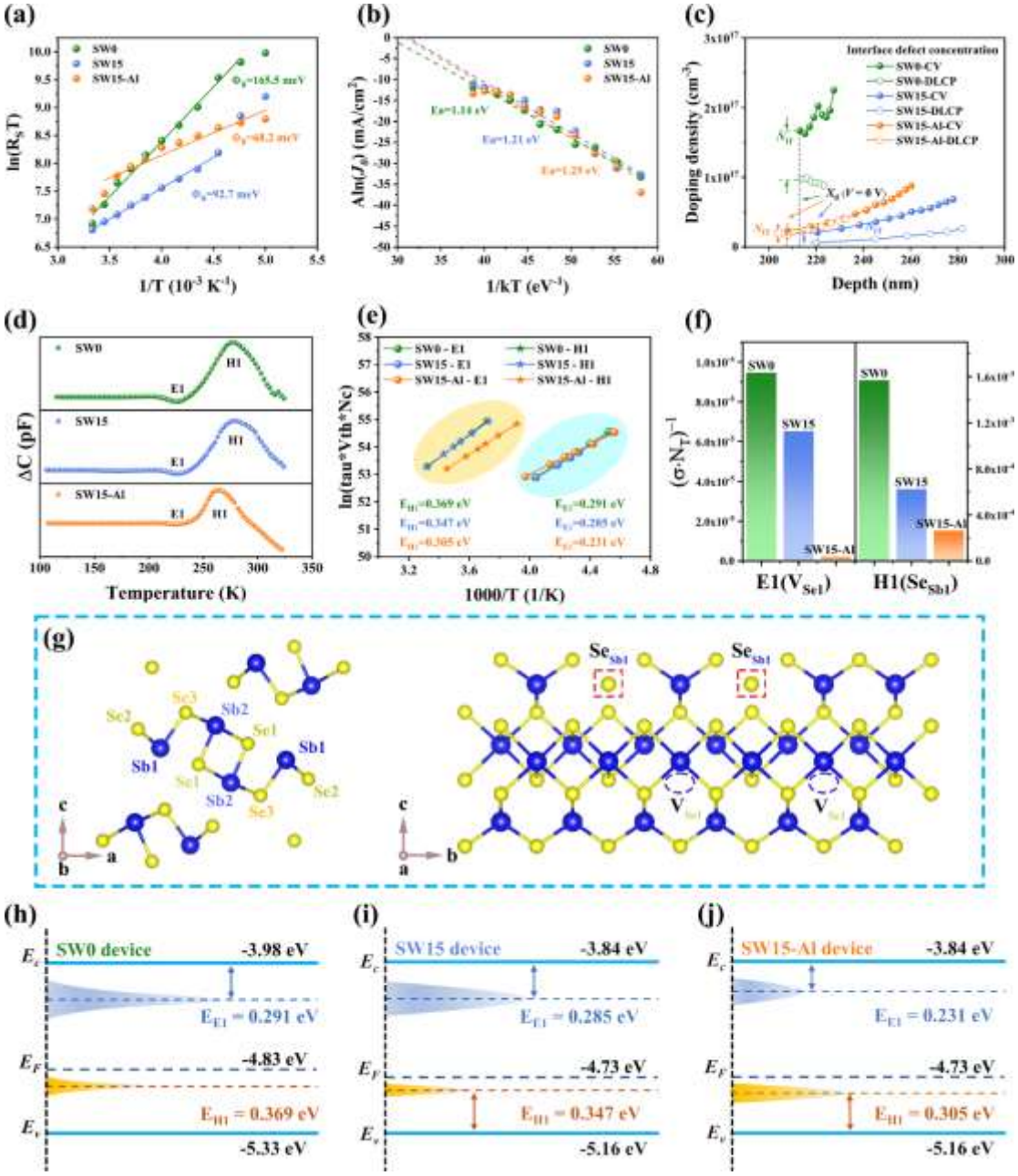

Fig. 5 Photoelectric properties and trap state investigation. (a) Blocking contact barrier height determination of the devices via temperature-dependent *J-V* measurement. (b) *A*ln(J_0) vs 1/kT plot of three devices. (c) *C-V* and DLCP profiling. (d) DLTS signals from the three devices. (e) Arrhenius plots obtained from DLTS signals. (f) Histogram of the calculated $(\sigma \cdot N_T)^{-1}$ values of traps in three devices. (g) The lattice of quasi-1D Sb_2Se_3 and the possible position of H1 (Se_{Sb1}) and E1 (V_{Se1}) defects in Sb_2Se_3 lattice. Schematic diagram of energy band and defect level of (h) SW0 device, (i) SW15 device, and (j) SW15-Al device.

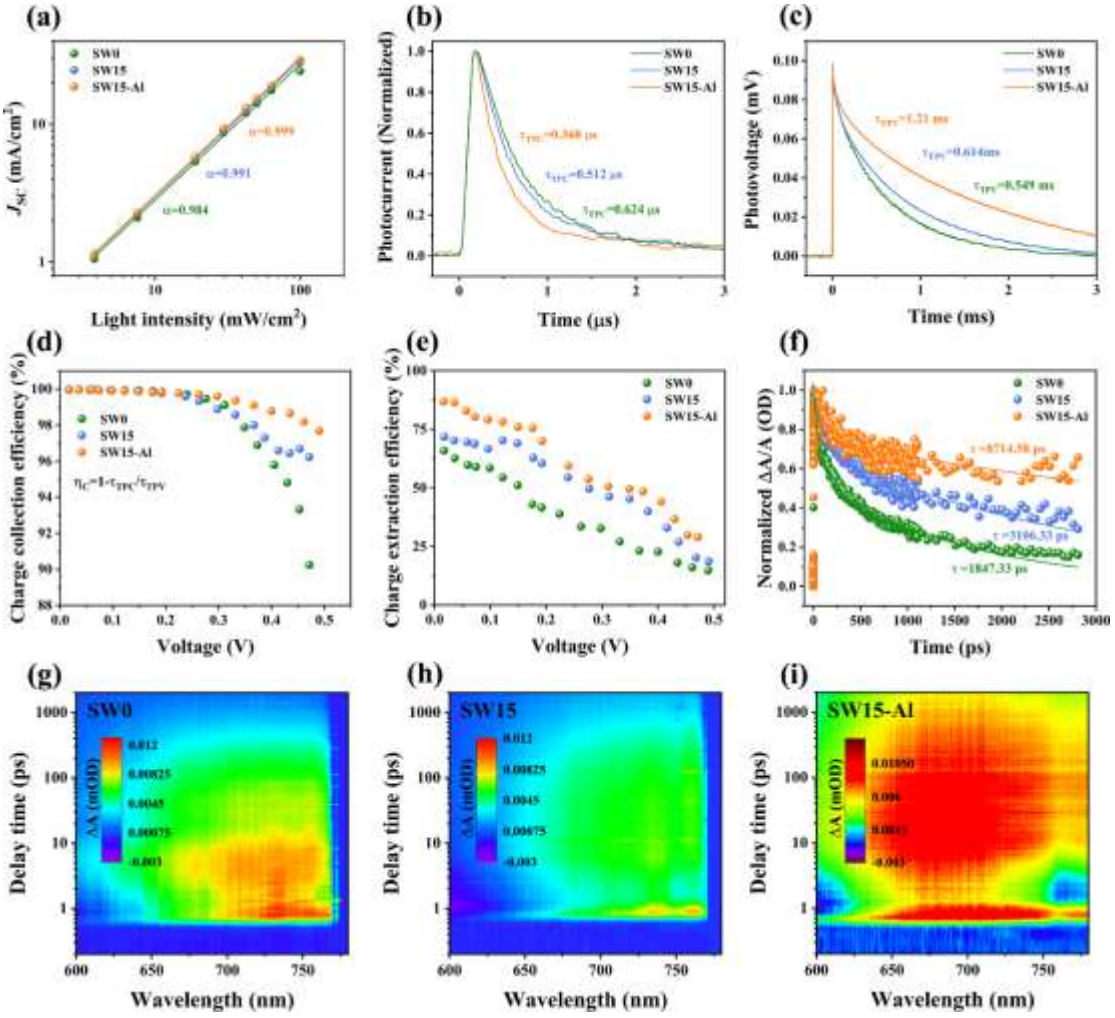

Fig. 6 Carrier dynamics analysis. (a) The dependence of J_{SC} on different light intensities of the three devices. (b) TPC and (c) TPV curves of the three devices. Bias voltage-dependent (d) η_C and (e) η_{ext} of the three devices. (f) Transient kinetic traces showing the decay of the PIA peak at 720 nm for both thin films. (g)-(i) TAS mapping of the SW0 sample, SW15 sample, and SW15-Al sample, respectively.

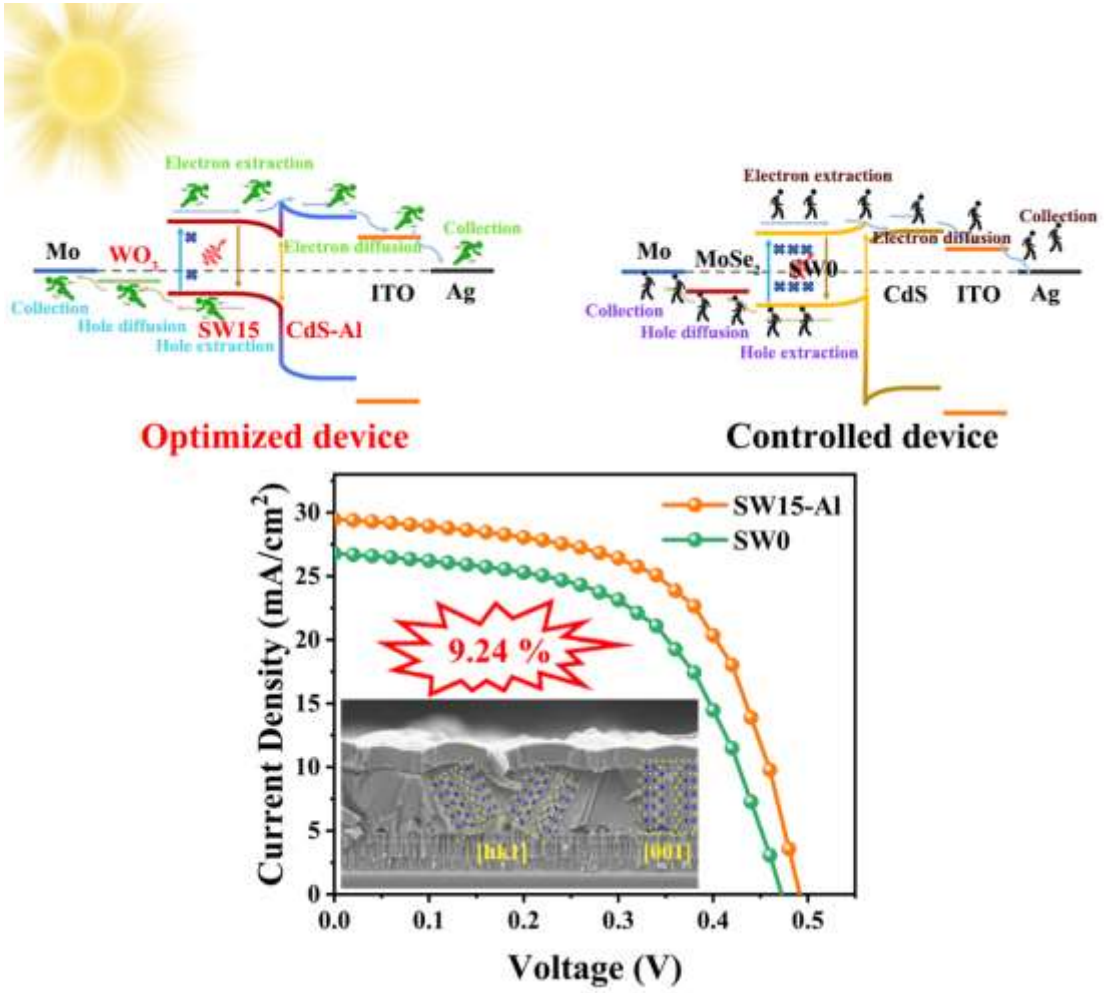

TOC

In this work, we synergistically employ buried interface and heterojunction engineering to regulate the film growth and optimize the band alignment. Thus, the interfacial trap-assisted non-radiative recombination loss has been successfully minimized, and heterojunction band alignment has been optimized. Hence, the champion device presents a PCE of 9.24%, representing the highest efficiency in sputtered-derived Sb_2Se_3 solar cells.